# RANS Simulations of a Calm Buoy in Regular and Irregular Seas using the SWENSE Method

C. Monroy, G. Ducrozet, F. Bonnefoy, A. Babarit, L. Gentaz, P. Ferrant

HAL Id: hal-01145146

https://hal.science/hal-01145146

Submitted on 24 Apr 2019

# RANS Simulations of a Calm Buoy in Regular and Irregular Seas using the SWENSE Method

*C. Monroy, G. Ducrozet, F. Bonnefoy, A. Babarit, L. Gentaz, P. Ferrant*

Laboratoire de Mécanique des Fluides/EHGO (UMR CNRS 6598)
Ecole Centrale de Nantes,
Nantes, France

## ABSTRACT

This paper presents recent advances of the SWENSE (Spectral Wave Explicit Navier-Stokes Equations) approach, a method for simulating fully nonlinear wave-body interactions including viscous effects. Potential flow theory is used to compute the incident waves while viscous effects are taken into account by using a Reynolds Averaged Navier-Stokes Equations (RANSE) solver to obtain the diffracted field in the full domain. Arbitrary incident wave systems can be described, including regular, irregular waves, multidirectional waves and focused wave events. The model may be fixed or moving with arbitrary speed and 6 degrees of freedom motion.

This paper presents the results of the SWENSE method for a captive calm buoy in various sea states (regular waves, 2D and 3D irregular waves). Results of the present approach compare favorably with experimental data.

KEY WORDS: RANS Equations; potential flow; nonlinear flow; combined approach; wave-body interactions; HOS model; SWENSE method.

## INTRODUCTION

Performance and seakeeping predictions are usually carried out in towing tank. However, in ship hydrodynamics, Computational Fluid Dynamics (CFD) is more and more used as a practical design tool. Main advantages of CFD are cost and time reduction as well as easier access to detailed flow field information. The complexity of simulating the behaviour of a ship in seaways was historically overcome by separating the problem in many simpler analysis: resistance, propulsion, maneuvering and seakeeping. Although these aspects are strongly coupled, CFD tends to simulate each of these phenomena separately using adapted theories :

- Resistance and propulsion analysis are now often addressed using viscous flow solvers based on the solution of RANS Equations, because viscosity or flow separation effects play an important role in the physics of those phenomena.

- Maneuvering and seakeeping problems are still currently solved by potential flow theory which is less time consuming and enables an accurate and efficient account of wave propagation phenomena.

However neglecting viscous effects can lead to poor predictions especially for rolling motion or cases for which strong separation occurs. This is why a natural evolution for CFD is to try to address seakeeping and resistance problems within a unified approach by taking into account incident waves in performance predictions.

The classical method used to simulate the viscous flow around a ship advancing in head waves is to impose an incident wave field at the inlet boundary. It is modelled as velocity and pressure perturbations which are added to the uniform stream. These perturbations are usually derived from the linear potential flow solution for free-surface travelling waves. However such simulations require very large computing resources because grids must be very refined between the location of the structure and the outer boundaries of the domain. This is indeed necessary to propagate waves from the paddle to the structure with no noticeable damping. Moreover successive wave reflections on the body or on the paddle affect the incoming wave train and reduce the useable duration of the numerical simulation ; it is indeed very complicated to damp the diffracted field without modifying the incident waves.

Yet, to be fair, it must be said that RANSE seakeeping simulations of a ship advancing in head regular waves using this straightforward approach are realizable and have been presented in Weymouth *et al.* (2005) or more recently in Visionneau *et al.* (2008) showing good results compared to "state of the art" potential simulations. However, the generation of irregular wave trains or focused waves will be very problematic with this method, especially for 3D sea states.

To overcome these difficulties an original formulation is used here by modifying the initial problem in order to solve the diffracted flow only. This approach has previously been used in the frame of potential theory, by Di Mascio *et al.* (1994) or Ferrant (1996) in 3D cases. It consists in splitting all unknowns of the problem (potential and free-surface elevation) into the sum of an incident term and a diffracted term. The incident terms are described explicitly using a nonlinear potential flow model. Thus only the part of the grid in the vicinity of the structure needs to be refined. Far from the body a stretched grid allows an efficient damping of the diffracted flow.

In the method presented here called SWENSE (Spectral Wave Explicit Navier Stokes Equations), potential flow theory is used to compute the incident waves while viscous effects are taken into account by using a RANSE solver to obtain the diffracted field in the full domain. By using this approach it is possible to simulate various nonlinear incident waves in an efficient and accurate manner: regular wave trains, focused waves, irregular 2D or 3D sea states. Moreover, the useful part of the simulations becomes practically unlimited because the incident waves and the diffracted field are separated during computation so that it becomes quite simple to damp the diffracted field only at the boundaries of the domain.

This technique has been already successfully applied and validated in 3D cases, like a vertical cylinder in regular waves with very accurate results on forces and wave runups comparing to experiments (Gentaz *et al.* (2004)). The numerical procedure has been further developed to simulate the forward speed diffraction on a naval combatant (a DTMB Model 5415) in regular nonlinear head waves (Luquet *et al.* (2004)) showing accurate results for the diffracted field and the forces components as well as successful grid dependency tests. Moreover the efficiency and accuracy of the method was showed at the last CFD workshop (Luquet *et al.* (2005)). First computations for irregular seas have been undertaken for a fixed TLP platform (Luquet *et al.* (2007)), while a more detailed validation of the method against the experiment in the case of an extensively long 2 DOF simulation in irregular head waves has been achieved in (Monroy *et al.* (2009)).

The objective of the present paper is to show the capabilities of the method for an industrial case: a calm buoy in various sea states. Results in regular waves and head irregular waves will be presented ant the method will be validated in 3D irregular waves.

## NUMERICAL FORMULATION

### Theory

The original RANS Equations solver used for the implementation of the SWENSE scheme was initially developed by Alessandrini and Delhommeau (1995) to solve the viscous, turbulent and free surface flow around a ship with a forward speed. It employs a free surface tracking method. The classical set of RANS Equations has been rewritten in order to formulate a problem for the nonlinear, viscous diffracted flow. Primitive unknowns (cartesian components of velocity ($U^\alpha$) with $\alpha \in \{1, 2, 3\}$, pressure $P$ and free-surface elevation $h$) are decomposed as follows:

$$
\begin{cases}
U^\alpha = U_I^\alpha + U_D^\alpha \\
P = P_I + P_D \\
h = h_I + h_D
\end{cases}
\tag{1}
$$

Variables with the subscripts $I$ and $D$ represent incident and diffracted variables respectively.

### SWENS Equations

The previous decomposition is introduced in the set of initial RANS equations in cartesian coordinates, assuming that the incident wave flow fulfils Euler equations and non-linear free surface boundary conditions in potential flow theory:

- Continuity equation

$$
\frac{\partial U_D^i}{\partial x^i} = 0
\tag{2}
$$

- Momentum equation

$$
\frac{\partial U_D^i}{\partial t} + \left( U_I^j + U_D^j - \frac{\partial \nu_t}{\partial x^j} \right) \frac{\partial U_D^i}{\partial x_j} - (\nu + \nu_t) \frac{\partial^2 U_D^i}{\partial x_j{}^2} + \frac{1}{\rho} \frac{\partial P_D}{\partial x_i}
$$

$$
= -U_D^j \frac{\partial U_I^i}{\partial x_j} + (\nu + \nu_t) \frac{\partial^2 U_I^i}{\partial x_j{}^2} + \frac{\partial \nu_t}{\partial x^j} \frac{\partial \left( U_I^j + U_D^j \right)}{\partial x_i}
\tag{3}
$$

- Free surface kinematic condition

$$
\frac{\partial h_D}{\partial t} + U_D^1 \left( \frac{\partial h_D}{\partial x^1} + \frac{\partial h_I}{\partial x^1} \right) + U_D^2 \left( \frac{\partial h_D}{\partial x^2} + \frac{\partial h_I}{\partial x^2} \right) - U_D^3
$$

$$
= U_I^3 - \frac{\partial h_I}{\partial t} - U_I^1 \left( \frac{\partial h_D}{\partial x^1} + \frac{\partial h_I}{\partial x^1} \right) - U_I^2 \left( \frac{\partial h_D}{\partial x^2} + \frac{\partial h_I}{\partial x^2} \right)
\tag{4}
$$

- Free surface normal dynamic condition

$$
P_D - \rho g h_D = \rho g h_I - P_I - 2\rho (\nu + \nu_t) \frac{\partial U_I^i + \partial U_D^i}{\partial x^j} n_i n_j
\tag{5}
$$

- Free surface tangential dynamic conditions

$$
\begin{cases}
(n_j t_{1i} + n_i t_{1j}) \frac{\partial U_D^i}{\partial x^j} = -(n_j t_{1i} + n_i t_{1j}) \frac{\partial U_I^i}{\partial x^j} \\
(n_j t_{2i} + n_i t_{2j}) \frac{\partial U_D^i}{\partial x^j} = -(n_j t_{2i} + n_i t_{2j}) \frac{\partial U_I^i}{\partial x^j}
\end{cases}
\tag{6}
$$

We obtain a new set of equations (Eqs. (2) to (6)) called SWENS equations in which incident variables (dynamic pressure, velocities, free-surface elevations and their gradients) are explicit. Their values are directly computed at each time step from the kinematics and interface location of the incident flow. Then, the diffracted variables are the only remaining unknowns of the problem and are solved by the modified viscous flow solver.

Other boundary conditions include a no-slip condition on the hull:

$$
U_D^i = -U_I^i
\tag{7}
$$

On the farfield, the cancellation of the diffracted velocities is progressively imposed. This modified condition combined with a stretching of the grid, in order to create a so-called *numerical beach*, prevents efficiently from diffracted wave reflections and verifies the decay of the diffracted field far from the body.

### Turbulence Model

Finally, to close the previous equation set we use a classical $k - \omega$ turbulence model proposed by Wilcox (1988), introducing a specific dissipation rate $\varpi$ without low Re formulation requirement.

## INCIDENT WAVE MODELS

In order to apply the SWENSE method it is necessary to have access at each time step to all the characteristics of the incident field (velocities, pressure, free surface elevations). Two nonlinear models for the incident flow have been implemented in the present version of the code: one for 2D nonlinear regular incident wave trains and another to model irregular wave trains. Some attributes were essential in the choice of these two models. Especially, in the SWENSE method, values of the incident field will be possibly needed above the undisturbed incident free

surface, as the total free surface elevation can indeed be higher than the incident elevation. Both wave models described below give access to a regular continuation of the incident fluid flow above the incident free surface, allowing an effective implementation of the SWENSE scheme. Furthermore, the velocity field generated by these methods is infinitely derivable in the whole space and this continuity is essential for the implementation of the equations and the behaviour of the computations.

## Regular waves

An algorithm based on the stream function theory, initially proposed by Rienecker and Fenton (1981), has been implemented. This algorithm has been chosen as it can generate the solution of steadily progressing periodic waves on irrotational flow over a horizontal bed for a wide range of wavelength/depth ratios and steepnesses, in the limit of regular wave stability, with quasi-arbitrary accuracy. Figure 1 shows the axial velocity field, computed with the Fenton-Rienecker algorithm for given amplitude and wavelength, in order to demonstrate the continuity of the wave field under, through and also above the free surface.
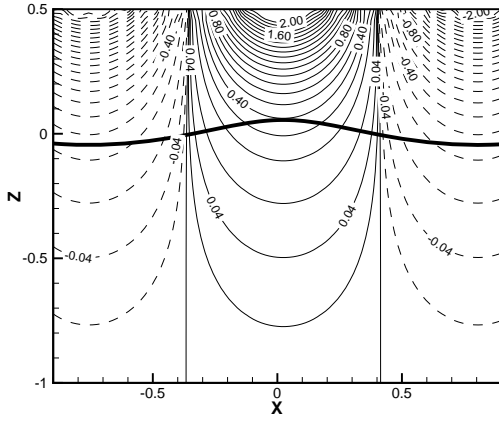


Figure 1: Contours of the axial velocity in the whole space for $2A$=0.1 m and $\lambda$=1.5 m. The bold line represents the free surface.

## Irregular waves

The model used in this configuration belongs to the family of Higher Order Spectral (HOS) schemes initiated by West *et al.* (1987) and Dommermuth and Yue (1987). This algorithm has been chosen as it can generate the solution of almost all the existing waves profiles on irrotational flow over a horizontal bed for any depth (in the limit of breaking waves) with huge accuracy (computer accuracy in fact) and fast computations. It is based on potential theory with nonlinear free-surface boundary conditions rewritten (following Zakharov (1968)) in terms of surface quantities, namely the single-valued free surface elevation $\eta(x, y, t)$ and the surface potential $\phi^s(x, y, t) = \phi(x, y, \eta, t)$:

$$\frac{\partial \phi^s}{\partial t} = -g\eta - \frac{1}{2}|\nabla\phi^s|^2 + \frac{1}{2}\left(1 + |\nabla\eta|^2\right)W^2 \qquad (8)$$

$$\frac{\partial \eta}{\partial t} = \left(1 + |\nabla\eta|^2\right)W - \nabla\phi^s.\nabla\eta \qquad (9)$$

on $z = \eta(x, y, t)$. $W = \frac{\partial \phi}{\partial z}$ is the vertical velocity. The unknows, $\eta(x, y, t)$ and $\phi^s(x, y, t)$, expressed at collocation points are time-marched once the vertical velocity has been obtained through the solution of a Dirichlet problem for the potential. The latter is solved by the HOS expansion of the potential in orders of the wave elevation

| | |
|---|---|
| Buoy diameter [m] | 0.920 |
| Buoy height [m] | 0.560 |
| Buoy draft [m] | 0.250 |
| Skirt diameter [m] | 1.100 |
| Skirt thickness [m] | 0.004 |
| Skirt location above keel [m] | 0.040 |

Table 1: Characteristics of the experimental model

in parallel with the order consistent formulation of West *et al.* (1987). Right hand sides of equations (8) and (9) contain nonlinear products which are computed in the spatial domain by means of a pseudospectral method. Rapid conversion between spectral and spatial spaces are made thanks to Fast Fourier Transforms (FFT). This leads us to a fully-spectral technique with a FFT-based resolution and a computational cost in $O(N\log(N))$ with $N$, the number of collocation points (which is equal to number of modes used in the spectral decomposition of the rectangular free-surface domain). Thus, the proposed method exhibits fast-convergence properties with very interesting computational time. The periodic formulation has been implemented as well as a new non-periodic one. The former gives the solution at large scale and the latter is useful to model a wave tank. For the details of the recent evolutions of the HOS method, you must refer to Ducrozet *et al.* (2006) and Bonnefoy *et al.* (2009).

## ILLUSTRATIVE APPLICATION

In 2004, an experimental campaign was conducted at the ECN wave basin and investigated the flow around a JIP calm buoy model. In this paper, we will compare the results of the SWENSE method against these experiments in the case of three different sea states: in regular head waves, in irregular head waves and in 3D irregular waves.

## Experimental set-up

The Centrale Nantes basin is 50 m long, 30 m wide and 5 m deep. One side is fitted with a bank of 48 flap-type wave generators while a parabolic absorbing beach is on the other side. The buoy model is placed at the centre of the basin in order to minimize the reflection effects from the basin walls.

The buoy shape is composed of a vertical circular cylinder equipped with a horizontal skirt close to the buoy keel. The characteristics of the buoy model can be found in table (1) and a view of the model is provided on Figure (2).



Figure 2: View of the experimental buoy.

In all the cases we have reproduced here, a framed structure keeps the buoy model captive. It is equipped with a dynamometer measuring the

efforts in the three directions. Five wave gauges are located at 1.150 m from the buoy centre and regularly spaced around a half circle. We will focus here on two surface elevations $\eta_1$ (gauge #1 is in front of the buoy with respect to the incoming waves) and $\eta_2$ (gauge #2 is also located upstream, at 45 degrees from the direction of the wave propagation). More exhaustive description of the experimental set-up can be found in Rousset *et al.* (2005).

## Numerical details

During this study, we have used different grids whose characteristics are given in Table (2). As the solver is based on finite-difference schemes, we use only structured meshes, and more specifically O-O grids. The columns *i*, *j* and *k* give the number of grid points in the three directions and $N_{tot}$ the total number of cells. $R_{dom}$ scales the radius of the mesh domain.

| | i | j | k | $N_{tot}$ | $R_{dom}$ (m) |
|---|---|---|---|---|---|
| Grid $R10N18$ | 39 | 72 | 65 | 182520 | 10.0 |
| Grid $R15N14$ | 33 | 77 | 56 | 142296 | 15.0 |
| Grid $R15N22$ | 39 | 89 | 65 | 225615 | 15.0 |
| Grid $R15N34$ | 45 | 102 | 75 | 344250 | 15.0 |
| Grid $R15N51$ | 51 | 117 | 86 | 513162 | 15.0 |

Table 2: Characteristics of the different grids.

Figure (3) provides a global view of the grid $R15N22$ with a large domain size of $R_{dom} = 15$m. The mesh is stretched in the farfield. This stretching combined to a canceling of the pressure is aimed at accurately damping all the diffracted terms (velocities, pressure and free surface elevations) in the outer part of the domain. A close-up view of the grid on the buoy can be observed on Figure (4). Grid refinements for an accurate computation of boundary layers are implemented all around the buoy and especially at the skirt in order to ensure a low y+ everywhere. Indeed, in all our computations in this study, the firsts cells of the grid on the buoy are inside the viscous sublayer with y+ always below 10.
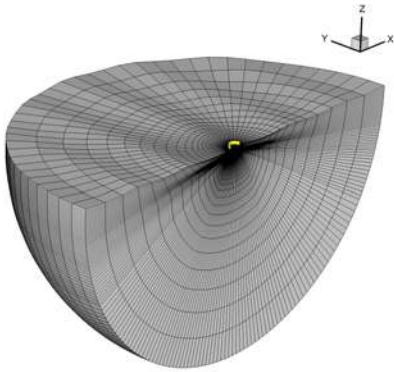


Figure 3: Global view of the mesh. Grid $R15N22$.

## Regular waves

Amongst the different regular wave trains which were generated during the experiments, we have focused on one specific case whose characteristics are the following: an amplitude $A = 0.0744$ m and a period $T = 1.8$ s. We have chosen this experimental run because the wavelength of the generated wave train ($\lambda = 5.05$ m) is close to the mean
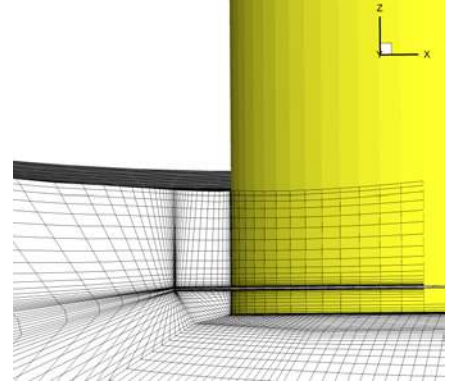


Figure 4: Close-up view of the grid on the buoy.

wavelength of the head irregular sea problem we study later in this article. It allows us to validate the size of the grid we use in order to avoid reflection of the diffracted field on the outer boundary. In the different computations we have performed for this regular wave train, we used a time step of 0.012 s, which makes 150 time steps per wave period. The forces are adimensionnalized, the drag and lift coefficients take the following form:

$$C_X(t) = \frac{F_X(t)}{Ak\rho g \nabla} \qquad (10)$$

$$C_Z(t) = \frac{F_Z(t)}{Ak\rho g \nabla} \qquad (11)$$

### Convergence study

We tried to follow the instructions of the ITTC, regarding the verification procedures for convergence studies. Between the grids $R15N14$, $R15N122$, $R15N34$ and $R15N51$, we used a refinement ratio $r_i = 1.15$ for the number of points in each direction each grid direction (i,j and k). It makes a refinement ratio of $r = 1.52$ for the total number of points $N_{tot}$, close to $r = \sqrt{2}$ suggested by the ITTC in its *recommended procedures and guidelines* for *Uncertainty Analysis in CFD, Verification and Validation, Methodology and Procedures*.

For every grid, 20 wave periods were computed (although only a few wave periods are necessary to reach a fully periodic steady state) with 150 time steps per wave period. On a single AMD Opteron 250 (2.4 GHz) processor, it takes from 3 hours per wave period for the grid $R15N14$ up to 18 hours per wave period for the grid $R15N51$. Tables (3) and (4) summarize the results of the convergence study. We focus on the first and second harmonics of the adimensionnalized forces ($C_X$, $C_Z$) and of two adimensionnalized surface elevations ($\eta_1$ and $\eta_2$). First, we can see that our method is very few grid-dependent, as the results do not vary much through the refinement process. For the finest mesh (grid $R15N51$), our first harmonic results are very close to the experimental values with an error of less than 4% (which is in the range of the experimental uncertainty). The second harmonics results for the forces are also satisfyingly predicted. However, we fail to get properly the second harmonics of the surface elevation.

In the table (3), we have added a comparison with Aquaplus, which is a state-of-the-art potential solver previously developped in our research department. Aquaplus uses linearized free surface conditions and works in the frequency domain. Its results for the first harmonics of the forces are significantly worse with errors of 25% for $C_X^{(1)}$ and 12% for $C_Z^{(1)}$.

| | $C_X^{(1)}$ | $C_X^{(2)}$ | $C_Z^{(1)}$ | $C_Z^{(2)}$ |
|---|---|---|---|---|
| Experiment | 1.39 | 0.17 | 1.18 | 0.015 |
| Aquaplus | 1.73 | | 1.04 | |
| | (+24%) | | (−12%) | |
| $R15N14$ | 1.42 | 0.165 | 1.15 | 0.010 |
| $R15N22$ | 1.42 | 0.165 | 1.15 | 0.010 |
| $R15N34$ | 1.42 | 0.165 | 1.16 | 0.010 |
| $R15N51$ | 1.405 | 0.16 | 1.14 | 0.010 |
| | (+1.0%) | (−6%) | (−3%) | (−33%) |

Table 3: Results for forces in regular head waves.

| | $\eta_1^{(1)}$ | $\eta_1^{(2)}$ | $\eta_2^{(1)}$ | $\eta_2^{(2)}$ |
|---|---|---|---|---|
| Experiment | 1.22 | 0.065 | 1.21 | 0.02 |
| $R15N14$ | 1.225 | 0.115 | 1.225 | 0.050 |
| $R15N22$ | 1.225 | 0.115 | 1.225 | 0.055 |
| $R15N34$ | 1.23 | 0.12 | 1.225 | 0.055 |
| $R15N51$ | 1.225 | 0.125 | 1.215 | 0.06 |
| | (+0.5%) | (+92%) | (+0.4%) | (+200%) |

Table 4: Results for surface elevations in regular head waves.

## *Vortex visualization*

Indeed, we chose this particular test case of a buoy with a skirt to emphasize the capabilities of the SWENSE method. As a matter of fact, the sharp geometry of the buoy induces complex viscous effects that only a viscous solver is able to compute efficiently. As an illustration, we show on Figure (5) the phenomenom of vortex-shedding which occurs at the skirt of the buoy. It is materialized by iso-surfaces of the Q-criterion. The Q-criterion (Eq. 12) was first defined in Hunt *et al.* (1988) and we recall here its expression:

$$Q = \frac{1}{2}\left(\left\|\overline{\overline{\Omega}}\right\|_E^2 - \left\|\overline{\overline{S}}\right\|_E^2\right) \quad (12)$$

where $\overline{\overline{\Omega}}$ and $\overline{\overline{S}}$ are the symmetric and antisymmetric components of $\nabla u$. Thus, Q represents the local balance between shear strain rate and vorticity magnitude. It is a convenient tool to visualize vortex structures.
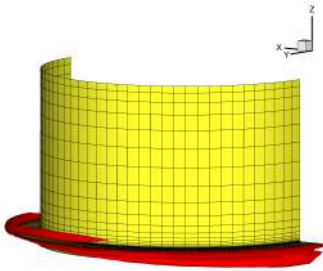


Figure 5: Iso-surfaces of $Q = 100\ m^2.s^{-2}$ at a random time step.

## **Irregular head waves**

The experimental wave spectrum consists in a Jonswap spectrum with a peak period $T_p = 2$ s, a significative height $H_s = 0.12$ m and $\gamma = 3$. The experimental run last 175 seconds and 150 seconds of it have been reproduced with the SWENSE method.

First, a 2D-HOS computation was realized with the same paddle-movement history as for the experiment for input. The HOS computation is rather fast compared to the SWENSE computation and took a few hours. For this case, we have used the $R15N22$ grid and a time step $\tau = 0.01$s (which makes 200 time steps per mean wave period). The whole computation took approximately three weeks on one AMD Opteron 250 (2.4 GHZ) processor. Figures (6), (7) and (8) show respectively the time history of $F_x$, $F_z$ and $\eta_2$ between 5 s and 50 s. Graphically, we observe a good accordance between the numerical and experimental signals. However, it is obvious that the accordance tends to detoriate during the simulation.
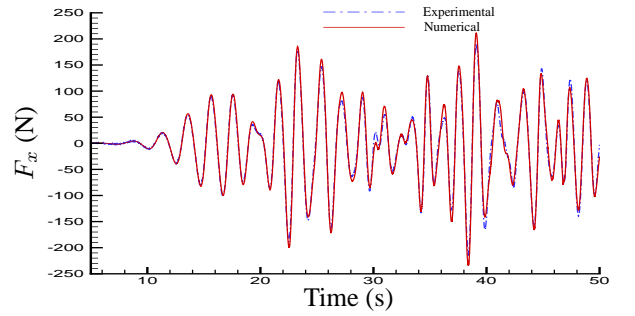


Figure 6: Time evolution of $F_x$ between 5 s and 50 s. Irregular head sea.
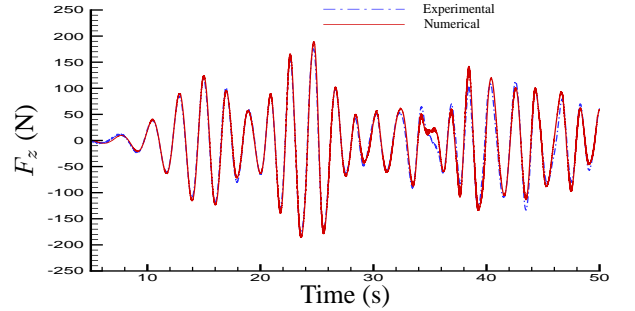


Figure 7: Time evolution of $F_z$ between 5 s and 50 s. Irregular head sea.

## *Comparison of the signal envelopes*

In this paragraph, we intend to compare the numerical and experimental signals and quantify their accordance all along the simulation. In order to introduce our comparator tool, we first consider two signals: $x^{simu}$(t) et $x^{expe}$(t), x can represent the elevation $\eta$ as well as the forces $F_x$ or $F_z$. Using the Hilbert transform, each of these two signals can take the following form:
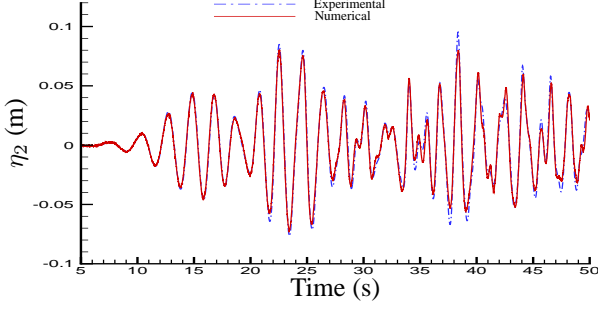
$$x\left(t\right) = a_x(t)cos(\phi_x(t)) \quad (13)$$

5

Figure 8: Time evolution of $\eta_2$, elevation at the probe 2, between 5 s and 50 s. Irregular head sea.

where $a_x$ ($a_x > 0$) and $\phi_x$ stand respectively for the amplitude envelope and the instantaneous phase of the signal x.

Figure (9) shows $a_{\eta_2}^{simu}(t)$ and $-a_{\eta_2}^{simu}(t)$ enveloping the signal $\eta_2^{simu}$, as well as $a_{\eta_2}^{expe}(t)$ and $-a_{\eta_2}^{expe}(t)$ enveloping the signal $\eta_2^{expe}$. In the same way, figure (10) shows the numerical and experimental envelope signals.
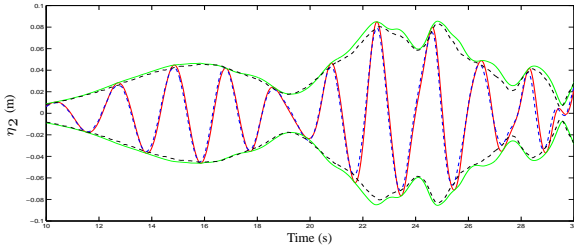


Figure 9: Time evolution of $\eta_2$ between 10 s and 30 s. Solid line: SWENSE signal and its envelope. Dashed line: experimenal signal and its envelope. Irregular head sea.
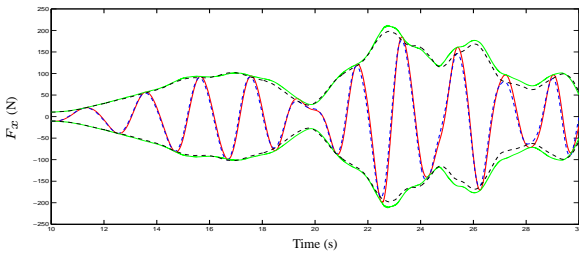


Figure 10: Time evolution of the force $F_x$ between 10 s and 30 s. Solid line: SWENSE signal and its envelope. Dashed line: experimenal signal and its envelope. Irregular head sea.

In order to quantify the evolution of the accordance between the simulation and the experiment, we have chosen to introduce the comparator tool $\zeta_x(\tau)$ defined by the equation 14.

$$\zeta_x(\tau) = \frac{\int_0^\tau \left| a_x^{expe}(t) - a_x^{simu}(t) \right| dt}{\int_0^\tau a_x^{expe}(t) dt} \qquad (14)$$

Geometrically, $\zeta_x$ scales the area between the numerical and the experimental envelopes divided by the area beneath the experimental envelope. Figure 11 shows the time evolution of the envelope ratio $\zeta_{F_x}$. $\zeta_{F_x}$ being important at the start of simulation is not significant and can be explained by the low envelope amplitudes and the small phase shift between the numerical and experimental signals.
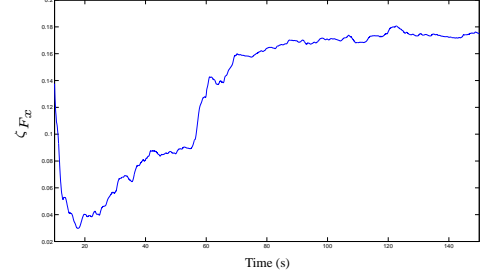


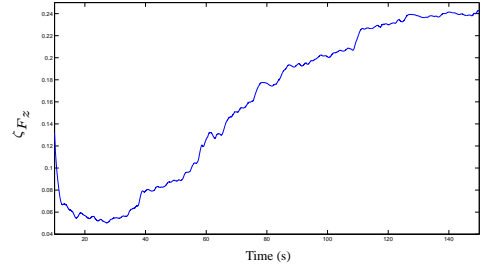Figure 11: Time evolution of $\zeta_{F_x}$. Irregular head sea.



Figure 12: Time evolution of $\zeta_{F_z}$. Irregular head sea.
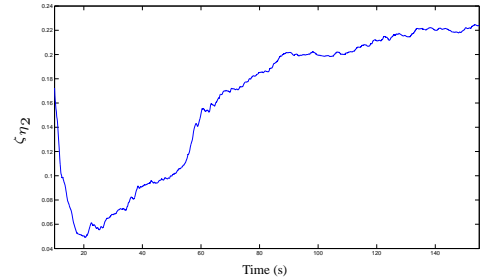


Figure 13: Time evolution of $\zeta_{\eta_2}$. Irregular head sea.

Around $t = 25$ s, we have an error rate $\zeta_{F_x}$ of $4.0\%$ between the simulation and the experiment for $F_x$ and an error rate $\zeta_{F_z}$ of $5.3\%$ for $F_z$. These results are very satisfying, but we observe a clear degradation of the accordance between the experiment and the simulation with error rates of approximately $10\%$ for $F_x$ and $F_z$ around $t = 55$ s.

It is difficult to know to what extent this progressive degradation is due to some numerical instabilities in our simulation or to the reflection effects of the diffracted waves on the walls of the basin during the experiment. These reflection effects are not taken into account in our HOS simulation (without a body) and can play a major effect as we saw in the post-processing of the experimental results for the regular waves.

Due to the dispersion relation, we can associate a mean group velocity $v_{g_m} \approx 1.57$ m.s$^{-1}$ to the peak period of the generated spectrum ($T_p = 2$ s). Both lateral basin walls are located at 14.5 m of the buoy, therefore it takes the waves $T_{AR} \approx 18.5$ s to go from the buoy to the walls and back from the walls to the buoy. As the front wave reaches the buoy at approximately $t = 8$ s, we should witness a degradation from 26.5 s. It coincides with what we can see on Figures 11, 12 and 13 with a degradation of the solution constantly increasing from approximately $t = 26$ s.

## Irregular 3D waves

The 3D irregular sea is composed of 2 superimposed Pierson-Moskowitz spectra: a swell sea coming from a direction $\theta = -22.5°$ with a peak period $T_p = 3$ s and a significative height $H_s = 6$ cm, a wind sea coming from a direction $\theta = 22.5°$ with $T_p = 1.5$ s and $H_s = 2$ cm. A 3D HOS computation was performed in a basin mode. The solver grid had then to fit entirely in the basin limits, that is why we used a small domain size of $R_{dom} = 10$ m. The grid $R10N18$ was doubled, as this case is not symmetrical. We used a time step $\tau = 0.05$ s (which makes 60 time steps per mean wave period if you consider the swell sea as predominant). The whole computation took approximately ten days on one AMD Opteron 250 (2.4 GHZ) processor.

Figures (14) and (15) show the time evolution of $F_y$ respectively between 10 s and 50 s and between 100 s and 140 s. The conformity of the experimental and numerical signals is qualitatively satisfying at the start of the simulation and although the accordance is obviously worse between 100 s and 140 s, both curves fit still well.
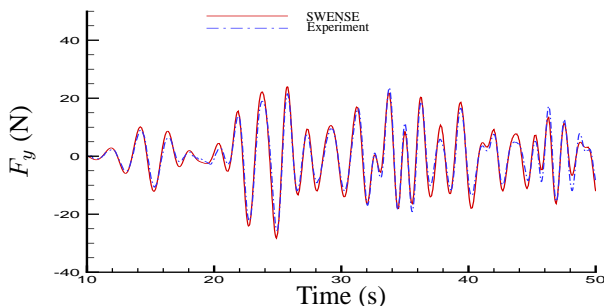


Figure 14: Time evolution of $F_y$ between 10 s and 50 s. 3D irregular sea.

Figure (16) summarizes the evolution of the $\zeta$ indicator for the forces $F_x$, $F_y$, $F_z$ and the elevation $\eta_2$. The overall behaviour of the accordance between the simulation and the experiment is similar to the 2D irregular case with a somewhat good accordance at the start (though not as good as in the 2D case) and a degradation along the simulation. After 30 seconds, $\zeta_{F_x}$ and $\zeta_{F_z}$ scale approximately 10% and $\zeta_{F_y}$ around 15%. Then, the results tend to detoriate, one can assume partly because of the come-back of diffracted waves from the basin walls in the experiment.

However, in this case, the accordance for the surface elevation is quite poor right from the start. $\zeta_{\eta_2}$ scales more than 25% at every moment and shows an even worse detoriation than the error rates for forces. The feet of the framed structure used to keep the buoy captive in the basin are not modeled in our computations. They may play a role in the poor accordance between the experimental and numerical elevations, as their effect on surface waves can not be neglected.
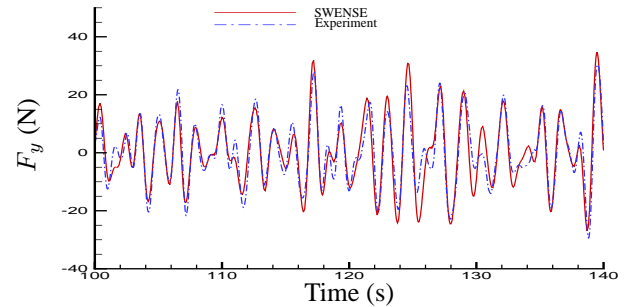


Figure 15: Time evolution of $F_y$ between 100 s and 140 s. 3D irregular sea.

## CONCLUSION

The illustrative application shows the potentialities of the SWENSE method. Strong viscous effects such as vortex shedding, produced by the sharp geometry of the model, are efficiently catched by the solver, and results for forces and elevations compare very well in the regular case. The method appears to be very few grid-dependent, which allows to perform trustworthy computations on relative light meshes and with low CPU time requirements. Both 2D and 3D irregular sea states have been reproduced with the HOS model. The characteristics of accuracy and efficiency are maintained with this new wave model. The introduction of an error-rate tool has permitted to quantify the accordance between the computation and the experiment all along the simulation and the results compare also favourably in both these cases. Future work will include a parallelization of the code in order to fasten the computations.

## REFERENCES

Alessandrini, B. and Delhommeau, G. (1995). "A Multigrid Velocity-Pressure-Free surface Elevation Fully Coupled solver for Calculation of Turbulent Incompressible Flow Around a Hull", 9th *International Conference on Numerical Methods in Laminar and Turbulent FLows*, Atlanta, USA.

Bonnefoy, F. and Ducrozet, G. and Le Touze, D. and Ferrant, P. (2009). "Time domain simulation of nonlinear water waves using spectral methods", *Advances in Coastal and Ocean Engineering*, Vol.11, World Scientific, pp 129-164.

Di Mascio, A. and Landrini, M. and Lalli, F. and Bulgarelli, U. (1994). "Three Dimensional non linear diffraction around fixed structures", 20th *symposium on naval hydrodynamics*, Santa Barbara, USA.

Dommermuth, D. and Yue, D. (1987). "A high-order spectral method for the study of nonlinear gravity waves", *J. Fluid Mech*, Vol.184, pp 267-288.

Ducrozet, G. and Bonnefoy, F. and Le Touzé, D. and Ferrant, P. (2006). "Implementation and validation of nonlinear wave maker models in a HOS Numerical Wave Tank", *Int. J. Offshore Polar Eng.*, Vol.3, pp 161-167.

Ferrant, P. (1996). "Simulation of strongly non-linear wave generation and wave-body interaction using a $3D\ MEL$ model", 21st *symposium*
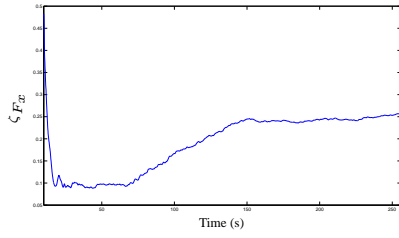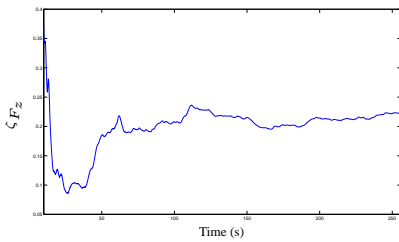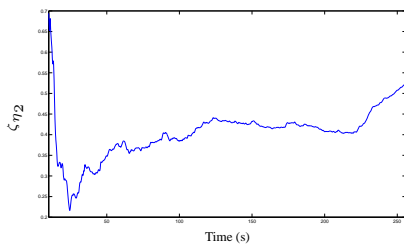
(a) $\zeta_{F_x}(t)$
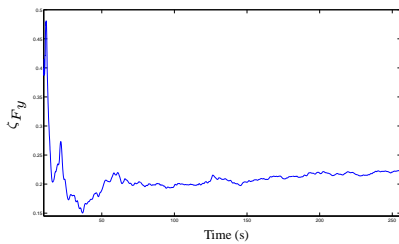


(b) $\zeta_{F_y}(t)$



(c) $\zeta_{F_z}(t)$



(d) $\zeta_{\eta_2}(t)$

Figure 16: Time evolution of $\zeta$ for the forces $F_x$, $F_y$, $F_z$ and the elevation $\eta_2$

*on naval hydrodynamics*, Trondheim, Norway.

Gentaz, L. and Luquet, R. and Ferrant, P. and Alessandrini, B. (2004). "Numerical simulation of a 3D viscous flow around a vertical cylinder in nonlinear waves using an explicit wave model", *International Conference on Offshore Mechanics and Arctic Engineering*, Vancouver, Canada.

Hunt, J. C. R., Wray, A., Moin, P. (1988). "Eddies, stram, and convergence zones in turbulent flows". *CTR-S88. Center for Turbulence Research*.

Luquet, R. and Alessandrini, B. and Ferrant, P. and Gentaz, L. (2004). "Simulation of the Viscous Flow Past a ship in Waves using the SWENSE approach", $25^{th}$ *ONR symp. on Naval Hydrodynamics*, St John's, Canada.

Luquet, R. and Jacquin, E. and Guillerm, P.E. and Gentaz, L. and Ferrant, P. and Alessandrini, B. (2005). "RANSE with free surface computations around fixed and free DTMB 5415 model, in still water and in waves", *CFD Workshop, Tokyo*.

Luquet, R. and Ferrant, P. and Alessandrini, B. and Ducrozet, G. and Gentaz, L. (2007). "Simulation of a TLP in Waves using the SWENSE scheme", *International Conference on Offshore Mechanics and Arctic Engineering*, San Diego, USA.

Monroy, C. and Ducrozet, G. and Roux de Reilhac, P. and Gentaz, L. and Ferrant, P. and Alessandrini, B. (2009). "RANS simulations of ship motions in regular and irregular head seas using the SWENSE method", *19th International Conference on Offshore and Polar Engineering*, Osaka, Japan.

Rienecker, M.M. and Fenton, J.D. (1981). "A Fourier approximation method for steady water waves", *Journal of Fluid Mechanics*, Vol.104, pp 119-137.

Rousset, J-M. and Ferrant, P. (2005). "Model tests for Principia R&D. CTR1 - JIP Calm Buoy 2". *Technical report, Laboratoire de mecanique des fluides de l'Ecole Centrale de Nantes (UMR CNRS 6598)*.

Visonneau, M. and Queutey, P. and Leroyer, A. and Deng, G.B. and Guilmineau, E. (2008). "Ship Motions in Moderate and steep Waves with an Interface Capturing Method", $8^{th}$ *International Conference on Hydrodynamics*, Nantes, France.

West, B. and Brueckner, K. and Janda, R. and Milder, M. and Milton, R. (1987). "A new numerical method for surface hydrodynamics", *J. Geophys. Res.*, Vol.92, pp 11803-11824.

Weymouth, G.D. and Wilson, R.V. and Stern, F. (2005). "$RANS$ Computational Fluid Dynamics Predictions of Pitch and Heave ship Motions in Head seas", *Journal of ship Research*, Vol.49(2), pp 80-97.

Wilcox, D.C. (1988). "Reassessment of the scale-determining equation for advanced turbulence models", *AIAA journal*, Vol.26, pp 1299-1310.

Zakharov, V.E. (1968). "Stability of periodic waves of finite amplitude on the surface of a deep fluid", *J. Appl. Mech. Tech. Phys.*, Vol.9, pp 190-194.